Talanta 297 (2026) 128690

Contents lists available at ScienceDirect

Talanta

journal homepage: www.elsevier.com/locate/talanta

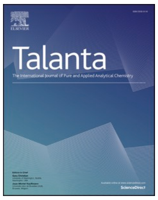

Glucose-activated cascade nanozyme hydrogels for synergistic antibacterial therapy via cascade reaction and microenvironment modulation in diabetic wounds

Wenbin Zhong [e,1], Dongying An [e,1], Zhiyu Ma [g,1], Jin Li [a], Nishan Jin [a], Yutian Zhou [e], Murui Ying [e], Xin Li [b,c,d], Song Gao [g,*], Bo Hu [f,**], Yang Zhang [a,b,***]

[a] *Shenyang Key Laboratory of Medical Molecular Theranostic Probes in School of Pharmacy, Shenyang Medical College, 146 Huanghe North Avenue, Shenyang, 110034, China*
[b] *Liaoning Province Key Laboratory for Phenomics of Human Ethnic Specificity and Critical Illness, Shenyang Medical College, 146 Huanghe North Avenue, Shenyang, 110034, China*
[c] *School of Stomatology, Shenyang Medical College, 146 Huanghe North Avenue, Shenyang, 110034, China*
[d] *Shenyang Key Laboratory of Prevention and Treatment of Systemic Important Diseases Associated with Oral Diseases, Shenyang Medical College, 146 Huanghe North Avenue, Shenyang, 110034, China*
[e] *School of Basic Medicine, Shenyang Medical College, 146 Huanghe North Avenue, Shenyang, 110034, China*
[f] *Department of Biochemistry and Molecular Biology, School of Life Sciences, China Medical University, Shenyang, 110122, China*
[g] *The Central Hospital of Shenyang Sujiatun, Shenyang, 110101, China*

ARTICLE INFO

Keywords:
Metal-organic framework
Nanozyme hydrogel
Antimicrobial therapy
Diabetic wound

ABSTRACT

Based on nickel metal-organic frameworks (Ni-MOF) and glucose oxidase (GOx), a self-activating cascade nanozyme hydrogel system (Ni-MOF@GOx-QT) was designed in this study to manage the dual challenges of bacterial control and tissue regeneration in the healing of infectious wounds. The hydrogel system incorporated the physical crosslinking of quaternized chitosan (QC) and tannic acid (TA) to create an injectable QT hydrogel encapsulating the Ni-MOF@GOx composite material. Within this system, GOx catalyzed the conversion of glucose into hydrogen peroxide (H_2O_2) and gluconic acid, triggering the peroxidase-like activity of Ni-MOF. This activity, enhanced by the lowered local pH, efficiently converted H_2O_2 into hydroxyl radicals (•OH), which exhibited potent antibacterial effects against both Gram-negative (*E. coli*) and Gram-positive bacteria (*S. aureus*). Additionally, characterization techniques, such as Search Engine Marketing (SEM), Transmission Electron Microscope (TEM), and X-ray Photoecectron Spectroscopy (XPS), confirmed the successful synthesis of the composite hydrogel, which demonstrated excellent biocompatibility and low cytotoxicity while promoting fibroblast migration and proliferation. In vitro experiments revealed a bacterial inhibition rate of more than 99 %. Furthermore, the hydrogel significantly accelerated the healing of infected wounds in a diabetic rat model. This research presents a novel, non-antibiotic-dependent, and microenvironment-responsive nanozyme hydrogel approach for treating diabetes-related infectious wounds, contributing to broadening the potential applications of nanozymes in biomedicine.

1. Introduction

Bacterial infections significantly impede wound healing. Traditional antibiotic treatments not only fail to provide lasting sterilization but also encourage the emergence of bacterial resistance. Diabetic wounds, characterized as persistent injuries associated with diabetes, present a highly intricate microenvironment. Elevated local glucose levels, up to 2–3 times higher than those in healthy skin, not only supply ample

---

* Corresponding author.

** Corresponding author.

*** Corresponding author. Shenyang Key Laboratory of Medical Molecular Theranostic Probes in School of Pharmacy, Shenyang Medical College, 146 Huanghe North Avenue, Shenyang, 110034, China.

E-mail addresses: lnsygs@yeah.net (S. Gao), bhu@cmu.edu.cn (B. Hu), zhangyangpro@symc.edu.cn (Y. Zhang).

[1] These authors contributed equally to this work.

https://doi.org/10.1016/j.talanta.2025.128690
Received 15 May 2025; Received in revised form 9 July 2025; Accepted 7 August 2025
Available online 8 August 2025

nutrients for bacterial growth, increasing infection risks, but also stimulate overproduction of reactive oxygen species (ROS) and reduce antioxidant capacity, resulting in oxidative stress imbalance. Hyperglycemia-induced vascular endothelial dysfunction leads to local wound hypoxia and inadequate nutrient provision, prolonging the inflammatory phase and impeding progression to the proliferative phase. The combination of multiple detrimental factors establishes a detrimental cycle, causing a significantly delayed healing process in diabetic wounds compared to normal wounds. In contrast to the typical healing period of 10 days for normal wounds, diabetic wounds exhibit a healing rate of only 78.99 % within 14 days. Additionally, neuropathy often renders patients insensitive to wound stimuli, further contributing to diagnostic and treatment delays. Consequently, there is a pressing need in contemporary research to develop innovative antibacterial materials that effectively kill bacteria and prevent the development of resistance. Research indicates that the pH of healthy skin is maintained within a slightly acidic range (pH 4–6), a condition also found in the environment of acute wounds [1–3]. Recently, nanozymes-new nanomaterials that exhibit enzyme-like catalytic properties-have garnered significant interest. These materials can produce bactericidal reactive oxygen species by mimicking the catalytic actions of natural enzymes [4,5]. Nanozymes with peroxidase-like (POD-like) activity, such as metals, metal oxides/sulfides, carbon materials (including carbon nanotubes, carbon dots, and graphene/graphene oxide), and metal-organic frameworks (MOFs), can transform exogenous hydrogen peroxide (H_2O_2) into highly reactive hydroxyl radicals (•OH) for bacterial infection treatment. Current research suggests that the bactericidal mechanism of nanozymes predominantly operates through the catalysis of highly oxidative •OH production [6,7]. However, this approach faces significant challenges in practical wound disinfection applications. First, the introduction of exogenous H_2O_2 may cause secondary damage and pain to the infected tissues. Second, the instability of H_2O_2 leads to its rapid decomposition, making the control of the externally added amount challenging and severely limiting its clinical utility.

The unique healing environment for diabetic patients merits attention due to its significant implications. Studies have shown that diabetic rats exhibit considerably higher blood glucose levels and skin glucose content both before and after injury, following similar trends as observed in previous clinical research. This research highlighted a strong correlation between the interstitial glucose levels in the skin of type II diabetes patients and their blood glucose concentrations. These findings underscore the necessity of carefully considering the high glucose microenvironments when developing nanozyme antibacterial materials for treating diabetic wounds. Furthermore, the elevated glucose concentration in these wound microenvironments provides abundant nutrients for bacterial growth, which in turn exacerbates infections and hinders the healing process. A promising treatment strategy, therefore, involves inhibiting bacterial growth by both cutting off their energy supply and consuming their nutrients. Glucose oxidase (GOx), a potent redox enzyme, plays a dual role in this context: it depletes glucose and oxygen in the wound, severing the bacteria's energy source, and it catalyzes the production of H_2O_2 and gluconic acid directly within the wound, thereby boosting antibacterial effectiveness [8,9]. This dual functionality makes GOx an exemplary candidate for developing advanced antibacterial materials. The H_2O_2 produced endogenously through GOx catalysis tackles the challenges associated with the external addition of H_2O_2 found in traditional antibacterial methods [10]. Additionally, gluconic acid, a byproduct and a weak acid, not only creates a conducive catalytic environment for POD-like nano materials but also enhances antibacterial efficacy by modifying the pH levels of the wound. Additionally, hydrogels, as intelligent soft materials with biophysical properties, are hydrophilic three-dimensional networks resembling biological tissues. They are significantly used in healthcare for drug delivery [11,12], tissue engineering [13,14], antimicrobial materials [15,16], and biosensors [17,18]. As a result, various ideal antimicrobial hydrogels have been developed to replace traditional antimicrobial agents, offering benefits such as low cost, ease of synthesis, good stability, localized release, single administration, excellent biocompatibility, and support in tissue repair [11,19]. Despite the significant promise shown by nanozyme systems based on GOx in antibacterial applications, fully leveraging this resource-rich antibacterial platform to achieve broad-spectrum, highly efficient bactericidal effects against Gram-positive, Gram-negative, and multidrug-resistant bacteria remains a critical scientific challenge that demands further in-depth exploration.

Building on this foundation, we developed a cascade reaction nanozyme system. Initially, a nickel metal-organic framework (Ni-MOF) material with POD-like activity was synthesized. GOx was then incorporated into the MOFs to create a nanozyme cascade system with outstanding POD-like and GOx activities. Moreover, leveraging the remarkable antibacterial properties of quaternary chitosan and tannic acid, an injectable QC-TA (QT) hydrogel was formulated. Subsequently, Ni-MOF@GOx was integrated into the QT hydrogel to create a Ni-MOF@GOx-QT nanozyme hydrogel. In bacterial-infected wounds, GOx crucially catalyzes the conversion of glucose in the wound environment into abundant gluconic acid and H_2O_2 [20,21]. This transformation yields dual antibacterial effects: the produced gluconic acid significantly lowers the local pH of the wound [22], enhancing the POD-like activity of Ni-MOF [23,24]. Additionally, the H_2O_2 generated by GOx catalysis can be further transformed into •OH under the catalyst of Ni-MOF, effectively killing bacteria by disrupting their cell membranes and biomolecules. This cascade catalytic reaction not only avoids the side effects associated with exogenous H_2O_2 addition but also significantly boosts antibacterial efficacy. Moreover, the Ni-MOF@GOx-QT nanozyme hydrogel promotes wound healing, and its injectable form alleviates excessive pressure on irregular wounds, making it particularly suitable for diabetic wounds. Hence, this nanozyme hydrogel, by initiating a dual-enzyme cascade system for antibacterial activity and synergizing with the antibacterial mechanism of the hydrogel, offers a distinct therapeutic strategy for the rapid healing of diabetic infected wounds.

2. Materials and methods

2.1. Synthesis of Ni-MOF

First, 1.0 g of $Ni(NO_3)_2$, 0.39 g of 2,5-dihydroxyterephthalic acid, and 0.1 g of cetyltrimethylammonium bromide (CTAB) were weighed and mixed in a beaker. Then, this mixture was added with 75 mL of N,N-Dimethylformamide (DMF), 5 mL of ethanol, and 5 mL of deionized water, and stirred for 20 min. Next, 100 μL of glacial acetic acid was introduced to ensure uniform blending, and the mixture was designated as the standard solution. Subsequently, this standard solution was transferred to a stainless steel high-pressure reactor, allowing for 24 h of reaction at 120 °C. After the reaction, the resultant product was washed three times with DMF and centrifuged at 10,000 rpm for 10 min to remove any residual solvents. Finally, the product was vacuum-dried at 80 °C.

2.2. Synthesis of Ni-MOF@GOx

Ni-MOF was dispersed in 15 mL of a sodium acetate buffer solution (NaAc, 50 mM, pH 5.1) and sonicated for 20 min. Subsequently, 10 mL of the NaAc buffer solution containing GOx (5 mg mL^{-1}) was mixed evenly with the dispersed Ni-MOF solution, followed by incubation at room temperature for 24 h. Next, the Ni-MOF@GOx biohybrid material was collected by centrifugation at 10,000 rpm for 15 min. The buffer washing steps were repeated three times. The encapsulation efficiency (*EE*) of GOx within Ni-MOF@GOx was determined using UV–vis spectroscopy. The *EE* was then calculated by measuring the absorbance of the supernatant after the initial centrifugation following encapsulation. equation (1) will be used to calculate the encapsulation efficiency of

GOx.

$$EE(\%) = \frac{W - W_1}{W} \times 100\% \tag{1}$$

Where W represents the total mass of GOx added to the Ni-MOF during encapsulation, and W_1 is the mass of unencapsulated GOx remaining in the supernatant, as determined from the standard curve.

2.3. Synthesis of QT hydrogels and Ni-MOF@GOx-QT nanozyme hydrogel

A 3 % (w/v, 30 mg mL^{-1}) QC solution (1 mL) was mixed with 300 μL of a 5 % (w/v, 50 mg mL^{-1}) TA solution and 200 μL of a 1 M NaAc solution (pH 4) and added with 100 μL of a 4 % (w/v, 40 mg mL^{-1}) sodium bicarbonate ($NaHCO_3$) solution. The mixed solution was immediately agitated.

2.4. POD-like activity evaluation of Ni-MOF@GOx

The catalytic activity of Ni-MOF@GOx, resembling that of POD, was evaluated by the 3,3′,5,5′-tetramethylbenzidine (TMB) colorimetric method. The procedure involved sequentially adding 15 μL of the Ni-MOF@GOx nanozyme solution (1000 μg mL^{-1}), 15 μL of TMB substrate solution (10 mM), and 15 μL of H_2O_2 solution (100 mM) to 255 μL of PBS buffer (10 mM, pH 7.4) in a standard reaction system, allowing for reaction at room temperature. Particularly, the changes in the characteristic absorption peak of the oxidized TMB at 652 nm were monitored by a UV–vis spectrophotometer for quantitative analysis of catalytic activity. Additionally, a comprehensive assessment of the catalytic performance of Ni-MOF@GOx was conducted by systematically investigating the influence of key parameters such as nanozyme concentration, pH, and temperature on catalytic activity.

2.5. Evaluation of GOx-like activity of Ni-MOF@GOx

At room temperature, 15 μL of Ni-MOF@GOx (1000 μg mL^{-1}), 15 μL of TMB (10 mM), and 30 μL of glucose (100 mM) were added sequentially to 240 μL of PBS buffer (10 mM, pH 7.4). Then, the changes in absorbance at 652 nm were monitored. Furthermore, the impact of critical parameters such as nanozyme concentration, pH, and temperature on the catalytic activity was examined systematically.

2.6. Evaluation of POD-like activity reaction mechanism

To further elucidate the reaction mechanism underlying the POD-like activity of Ni-MOF, isopropyl alcohol (IPA) was employed as a hydroxyl radical scavenger. IPA can bind to hydroxyl radicals, thereby inhibiting the POD-like reaction. Varying concentrations of IPA were added under optimal reaction conditions, and changes in the absorbance at 652 nm were monitored. Electron paramagnetic resonance (EPR) spectroscopy was utilized with 5,5-dimethyl-1-pyrroline N-oxide (DMPO) as a spin trap to directly detect radical species, confirming the reaction mechanism of Ni-MOF.

2.7. Assessment of hydrogel properties

Adhesion testing of hydrogels. The adhesion properties of the Ni-MOF@GOx-QT nanozyme hydrogel were tested on human skin and various materials including glass and plastic. The results were documented by optical images.

Injectability testing of hydrogels. The injectability of the Ni-MOF@GOx-QT nanozyme hydrogel was evaluated through injection molding. The hydrogel was loaded into a syringe and manually extruded to create various shapes, comprising different letters. Optical images of these shapes were captured.

Swelling testing of hydrogels. The swelling behavior of both the QT hydrogel and the Ni-MOF@GOx-QT nanozyme hydrogel was investigated with the swelling ratio (SR) as a metric. Specifically, the dry mass of the hydrogel samples (W_d) was measured and immersed in a PBS buffer (pH 7.4), the samples were withdrawn at specified time intervals at 37 °C, surface moisture was delicately removed with filter paper, the swollen mass (W_t) was recorded. The SR was calculated using equation (2):

$$SR\,(\%) = \frac{W_d - W_t}{W_t} \times 100\% \tag{2}$$

2.8. Evaluation of antimicrobial activity in vitro

Bacterial activation and suspension preparation. Standard nutrient agar and nutrient broth were prepared according to their respective recipes, sterilized in an autoclave at 121 °C for 30 min, and then allowed for cooling to 70 °C. *Escherichia coli* (*E. coli*) and *Staphylococcus aureus* (*S. aureus*) were selected as the model bacterial strains. For activation, the frozen bacterial strains stored at −20 °C were inoculated into 50 mL of sterile nutrient broth. After thawing at room temperature, 50 μL of the bacterial suspension was transferred to a fresh nutrient medium and incubated at 37 °C, followed by shaking at 200 rpm for 12–16 h. Increased turbidity in the broth confirms the successful bacterial activation and demonstrates readiness for subsequent experiments.

Assessment of antimicrobial efficacy. Evaluation of Ni-MOF@GOx antimicrobial efficacy: A bacterial stock solution (2×10^9 CFU mL^{-1}) was diluted to 2×10^4 CFU mL^{-1} to evaluate the sterilization performance of the material. Then, 0.05 mL of bacterial suspension (1×10^5 CFU mL^{-1}) was sequentially mixed with Ni-MOF@GOx (5 mg mL^{-1}), H_2O_2 (10 mM), NaAc buffer (100 mM), and PBS buffer (10 mM, pH 7.4). This mixture was diluted to a final volume of 0.5 mL with medium and incubated for 20 min. Afterward, 0.1 mL of the mixture was evenly spread onto prepared agar plates by a sterile spreader and incubated at 37 °C for 18 h. After incubation, the number of bacterial colonies was counted to determine microbial quantity and growth. The bacteriostatic or bacterial survival rate for each group was calculated as. Equations (3) and (4) were used to calculate the bacteriostatic and bacterial survival rates for each group:

$$Bacteriostatic\ rate\ (\%) = \frac{Number_{sample}}{Number_{control}} \times 100\% \tag{3}$$

$$Bacterial\ survival\ rate\ (\%) = \frac{Number_{control} - Number_{sample}}{Number_{control}} \times 100\% \tag{4}$$

Evaluation of antimicrobial efficacy of QT and Ni-MOF@GOx-QT: The antibacterial properties of QT hydrogel and Ni-MOF@GOx-QT nanozyme hydrogel (with Ni-MOF@GOx at 50 μg mL^{-1}) were evaluated by a standard plate counting method. Each 200 μL sample of sterile hydrogel was mixed with an equal volume of bacterial suspension (≈10^6 CFU mL^{-1}). PBS-treated groups served as negative controls. These mixtures were incubated at 37 °C for 24 h. Following incubation, 100 μL of each bacterial solution was serially diluted and spread evenly on nutrient agar plates. After further incubation at 37 °C for 24 h, bacterial colony-forming units were counted by a colony counter. The bacterial survival rates were calculated, and each experiment was conducted in triplicate.

2.9. Cytotoxicity assay

The compatibility of hydrogel materials with cells was evaluated through the CCK-8 assay. The procedure was detailed as follows. First, mouse fibroblast cells (L929) were seeded in a 96-well plate at a density of 20,000 cells per well. Each well received 200 μL of complete culture medium supplemented with various concentrations of the hydrogel extract. A treatment group with only PBS served as a negative control.

The cells were incubated in a 5 % CO_2 humidified incubator at 37 °C for 24 h. After incubation, the medium was carefully removed from each well, with 200 μL of 10 % CCK-8 solution added. The cells were incubated for an additional 0.5–4 h under the same conditions. Besides, the absorbance at 450 nm (OD_{450}) was measured to assess cell viability. The viability was calculated by equation (5):

$$Cell\ viability\ (\%) = \frac{OD_{sample} - OD_{blank}}{OD_{control} - OD_{blank}} \times 100\% \tag{5}$$

Cell proliferation. The cell proliferation assay involved seeding a 200 μL suspension of fibroblasts (1000 cells per well) in a 96-well culture plate. After cell adhesion, the medium was removed from each well. The experimental group was treated with a composite hydrogel extract, while the control group received an extract without the composite hydrogel. Particularly, the plate was placed in a 37 °C, 5 % CO_2 incubator for 24, 48, and 72 h. At each time point, the medium was aspirated, and the wells were washed twice with PBS. Subsequently, 200 μL of 10 % CCK-8 solution was added to each well, with further incubation for 0.5–4 h. OD was recorded at 0.5, 1.0, and 2.0 h to maintain the OD value around 1.0. The OD values at 450 nm were measured by a microplate reader to generate a proliferation curve.

Cell scratch repair. The cell scratch repair assay was conducted on a 6-well plate. Fibroblasts were seeded at a density of 500,000 cells per well in the control group, QT hydrogel group, and Ni-MOF@GOx-QT nanozyme hydrogel group. After 24 h, scratches were made vertically by a sterile 200 μL pipette tip when the cells reached confluence. Subsequently, the cells were washed three times with PBS to remove any detached cells, followed by incubation in DMEM either serum-free or containing 0.5 % fetal bovine serum to minimize the effects of serum on cell proliferation. Cell migration was observed under a microscope at 12 and 24 h post-scratch and analyzed through ImageJ software.

Hemolysis assay. With the purpose of preparing the extract from the hydrogel, PBS was added to the hydrogel, followed by incubation at room temperature for 24 h. Then, the in vitro hemolysis assay was conducted through a suspension of red blood cells from SD rats. The rats were anesthetized with isoflurane gas and placed in an anesthesia chamber. Afterward, fresh whole blood was collected and centrifuged at 1500 rpm to separate the red blood cells, which were washed repeatedly with saline until the supernatant appeared clear. Subsequently, these cells diluted to generate a 2 % red blood cell suspension. Regarding the assay, 0.3 g of hydrogel and 2 mL of the prepared red blood cell suspension were sequentially added to a test tube. The mixture was co-incubated for 3 h. Control groups were established in the experimental setup, using water and saline as the positive and negative controls, respectively. After incubation, the samples were centrifuged to separate the supernatant, and the absorbance of 540 nm was measured. The hemolysis rate (*HR*) was calculated by equation (6):

$$HR\ (\%) = \frac{A - A_0}{A_{100} - A_0} \times 100\% \tag{6}$$

Where A, A_0, and A_{100} denote the absorbance values at 540 nm for the experimental group (treated with the nanozyme hydrogel), the negative control group (saline), and the positive control group (complete hemolysis), respectively.

2.10. Evaluation of wound healing

Diabetic skin injury model. Male Sprague-Dawley rats, aged 6–8 weeks, were utilized for this study. Upon arrival, the rats acclimatized for three days following transportation. The animals were divided into three groups, with each group consisting of five rats. All rats were male SPF-grade SD rats, weighing 200–220 g. The groups included a control group, a QT hydrogel group, and a Ni-MOF@GOx-QT nanozyme hydrogel group. All rats were fed a high-fat diet for four weeks. This was followed by an intraperitoneal injection of STZ administered daily for three consecutive days at a dose of 80 mg kg^{-1}. Fasting blood glucose levels were measured three days after the final injection. Rats displaying blood glucose levels above 16.7 mmol L^{-1} were considered to have been successfully induced with diabetes. Following diabetes induction, skin injury models were created on all rats. The animals were anesthetized using an isoflurane gas anesthesia machine, maintaining a 1.5 % concentration. After achieving anesthesia, the rats were positioned prone on a surgical drape. The back hair was removed using depilatory cream and a shaver, focusing on a 4 × 4 cm area. The area was then disinfected with iodine and subsequently deiodinated using 75 % ethanol. A circular full-thickness skin defect with a diameter of 1.5 cm was created using a puncher, exposing the wound. Any adhesions were carefully trimmed with scissors. Hemostasis was achieved by applying pressure with cotton balls immediately after creating the wound. Post-wound creation, the control group continued to receive their regular diet, while the QT hydrogel group and the Ni-MOF@GOx-QT nanozyme hydrogel group received daily applications of their respective treatments directly to the wound for 14 days. The weights of the rats were recorded on days 0, 3, 7, 10, and 14 of treatment. Prior to each imaging session, any new hair growth around the wound was cleared to ensure it did not interfere with the imaging results. Wound photographs were taken, and the software was utilized to measure the wound area for each group. The wound healing rate (*WHR*) was calculated using the following formula (7):

$$WHR\ (\%) = \frac{S_n - S_0}{S_n} \times 100\% \tag{7}$$

S_0 and S_n represent the initial wound area on day 0 and the wound area on day n (where n = 3, 7, 10, and 14), respectively.

2.11. Tissue pathology assessment

In this study, a standardized process was established for histopathological evaluation in assessing wound healing. Full-thickness skin tissue samples were systematically collected at various postoperative intervals (0, 3, 7, 10, and 14 days), fixed in a 4 % paraformaldehyde solution, dehydrated, and then embedded in paraffin. Subsequently, sections of 4 μm thickness were prepared by a rotary microtome and mounted on glass slides after being oven-dried at 60 °C. Concerning staining, both Hematoxylin and Eosin (HE) and Masson's Trichrome staining kits were employed as per the manufacturer's instructions. With specialized image analysis software, digital images of all stained sections were captured with an optical microscope system and analyzed for morphological changes.

3. Results and discussion

3.1. Synthesis and characterization of materials

SEM images of Ni-MOF and Ni-MOF@GOx are displayed in Fig. 1A and B, respectively. Ni-MOF shows a uniform spindle-shaped microstructure where individual particles cluster together to form cauliflower-like, three-dimensional structures. This morphology demonstrates excellent control over shape and uniformity in Ni-MOF. Upon the addition of GOx, the particle size of Ni-MOF@GOx increases slightly, yet it retains the spindle shape and clustered, cauliflower-like structure, indicating that the GOx loading has minimal impact on the fundamental microstructure of Ni-MOF. The increase in particle diameter after GOx loading may be attributed to the formation of a denser coating layer on Ni-MOF's surface by GOx, which enhances particle aggregation and size. A TEM image, shown in Fig. 1C, reveals the maintained spindle-shaped morphology of individual Ni-MOF@GOx particles. EDS images, depicted in Fig. 1D and F, confirm the uniform distribution of the Ni element within Ni-MOF@GOx. Additionally, the XRD pattern of Ni-MOF@GOx, illustrated in Fig. 1E, exhibits two distinct diffraction peaks at 2θ = 7.86° and 13.65°, which correspond to the (210) and (300) crystal faces, respectively, indicating that the topological structure of Ni-MOF is

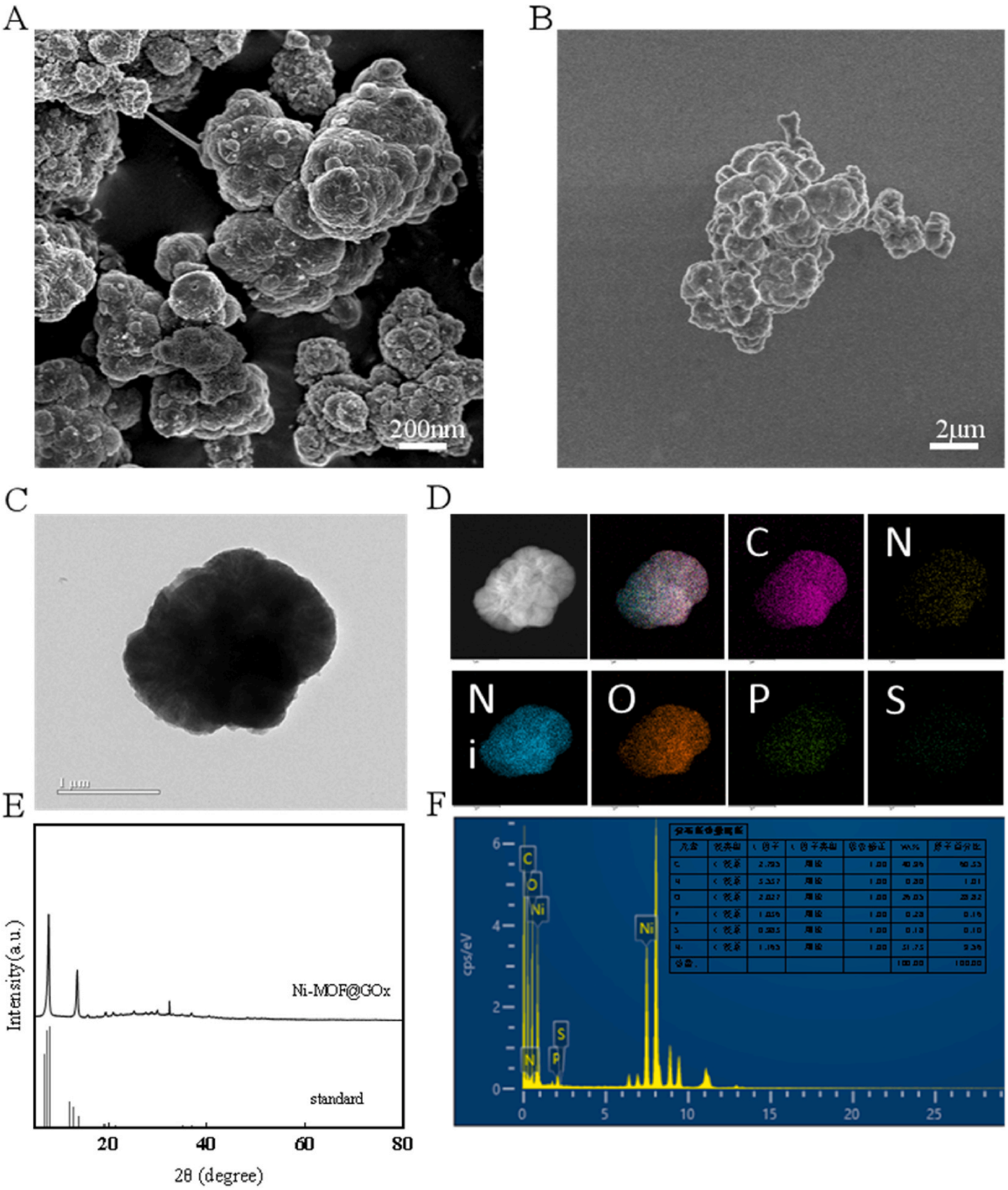

Fig. 1. SEM images of (A) Ni-MOF and (B) Ni-MOF@GOx. Panel (C) presents the TEM image of Ni-MOF@GOx. Panel (D) showcases the dark-field TEM image and EDS elemental mapping of Ni-MOF@GOx, with corresponding elemental maps of C, N, Ni, O, P, and S. Panel (E) illustrates the XRD spectra of Ni-MOF@GOx and the standard diffraction card. Panel (F) exhibits the EDS spectrum and elemental composition of Ni-MOF@GOx.

retained after loading with GOx. XPS analysis of Ni-MOF@GOx identified 6 principal components (Fig. S1A): C 1s (284.8 eV), N 1s (399.7 eV), O 1s (531.5 eV), Ni 2p (855.7 eV), P 2p (133.5 eV), and S 2p (163.2 eV). High-resolution XPS spectra of Ni 2p in Ni-MOF@GOx showed two peaks at 855.6 eV and 861.6 eV for Ni 2p3/2, and one peak at 873.3 eV and 880.7 eV for Ni 2p1/2, consistent with the characteristics of Ni^{2+} (Fig. S1E). This indicates the presence of Ni^{2+} in the composite [25], further verifying the successful synthesis of Ni-MOF@GOx. The composite also maintained its original morphology and porous framework after GOx loading, evidenced by its crystallographic features and unchanged microtopology. FT-IR spectra (Fig. S1H) revealed characteristic peaks at 2870 cm^{-1} and 2970 cm^{-1}, attributed to the asymmetric (ν_as CH_3) and symmetric (ν_s CH_3) C–H stretching vibration modes of methyl (-CH_3) groups in the GOx molecules [26,27], providing further evidence of successful GOx immobilization on Ni-MOF. The loading capacity of GOx in Ni-MOF@GOx was determined to be 20.7 ± 0.5 %, with a standard curve of $y = 0.4661x + 0.0023$ and $R^2 = 0.9932$.

3.2. Nanozyme activity assessment

The catalytic mechanism of Ni-MOF@GOx is depicted in Fig. 2A, which demonstrates its ability to achieve efficient antibacterial effects through a cascade reaction. Specifically, the GOx catalyst initially catalyzes the oxidation of glucose in the wound microenvironment, producing gluconic acid and H_2O_2. This reaction significantly lowers the local pH and increases the concentration of H_2O_2. Under these acidic conditions, Ni-MOF exhibits enhanced POD-like activity, efficiently converting H_2O_2 into toxic •OH, thereby achieving sterilization through an enzyme-cascade reaction. The POD-like catalytic activity of Ni-MOF@GOx was evaluated using TMB as a substrate, revealing that it maintains catalytic activity comparable to that of Ni-MOF alone (Fig. 2B and G). This indicates that the addition of GOx does not compromise the

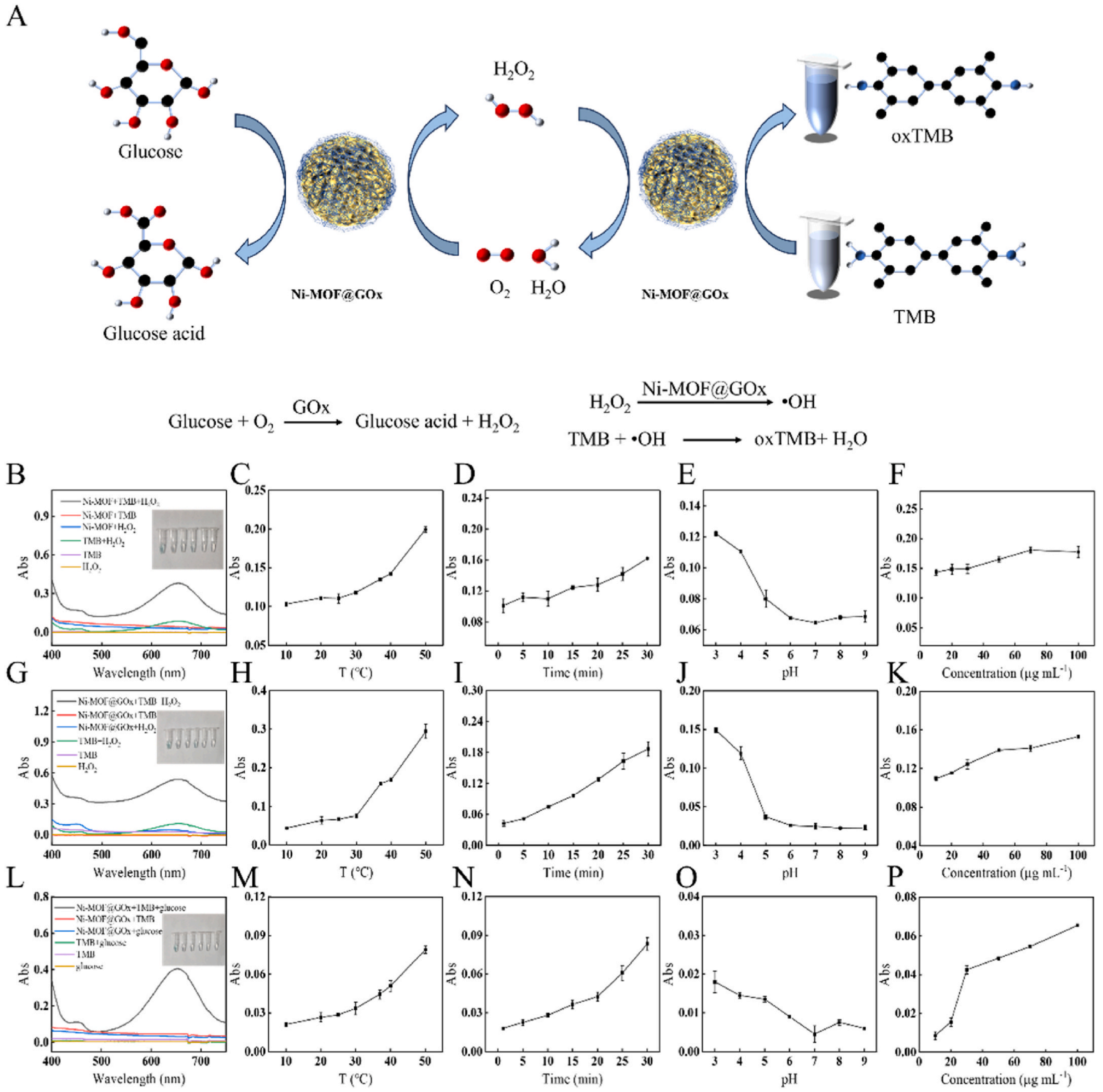

Fig. 2. The schematic diagram of the Ni-MOF@GOx cascade catalytic reaction (A) and the UV–vis spectrum of Ni-MOF with POD-like activity (B). The optimization of POD-like activity of Ni-MOF regarding temperature (C), time (D), pH (E), and Ni-MOF concentration (F). The UV–vis spectrum of Ni-MOF with POD-like activity (G). The optimization of POD-like activity of Ni-MOF@GOx in relation to temperature (H), time (I), pH (J), and Ni-MOF@GOx concentration (K). The UV–vis spectrum of GOx catalytic activity for Ni-MOF@GOx (L). The optimization of GOx activity for Ni-MOF@GOx regarding temperature (M), time (N), pH (O), and Ni-MOF@GOx concentration (P).

intrinsic POD-like activity of Ni-MOF. Moreover, the optimization of factors influencing the POD-like catalytic activity of Ni-MOF was conducted, including temperature (Fig. 2C), time (Fig. 2D), pH (Fig. 2E), and concentration of Ni-MOF (Fig. 2F). The optimal reaction conditions were determined to be a temperature of 37 °C, a duration of 20 min, a pH of 4.0, and a Ni-MOF concentration of 50 μg mL^{-1}.

The TMB method was also employed to assess the glucose-mimicking POD catalytic activity of Ni-MOF@GOx within the reaction system. Factors influencing the POD catalytic activity of Ni-MOF@GOx were optimized, including temperature (Fig. 2H), time (Fig. 2I), pH (Fig. 2J), and Ni-MOF concentration (Fig. 2K). The established optimal reaction conditions were as follows: temperature at 37 °C, duration of 20 min, pH at 4.0, and Ni-MOF@GOx concentration of 50 μg mL^{-1}. Ni-MOF@GOx displayed superior enzyme-like activity and stability compared to Ni-MOF alone, likely due to the nano-confinement effect within the MOF, which effectively prevents the denaturation and aggregation of GOx [28], thereby enhancing the enzyme's stability across various environments [29]. Despite the decrease in pH resulting from the catalysis of glucose to gluconic acid by GOx, the material exhibited higher absorption peaks at pH 3–4, which gradually decreased with an increase in pH

(Fig. 2O). The POD-like activity of Ni-MOF@GOx under pH conditions of 3–4 showed no significant change compared to that of Ni-MOF alone (Fig. 2E and J). Additionally, the conditions affecting the glucose oxidation capability of Ni-MOF@GOx were optimized, including temperature (Fig. 4M), time (Fig. 2N), and Ni-MOF@GOx concentration (Fig. 2P). The optimal conditions were determined to be a temperature of 37 °C, a duration of 20 min, a pH of 4.0, and a Ni-MOF@GOx concentration of 50 μg mL^{-1}.

3.3. Determination of POD-like activity reaction mechanism

In the Ni-MOF POD-like reaction system, the absorbance values at 652 nm decreased progressively with the addition of 0 mM, 0.1 mM, 1 mM, and 1.5 mM IPA (Fig. S2A). Additionally, an EPR spectrum displayed a symmetrical peak with a relative intensity ratio of 1:2:2:1 when DMPO was used in a radical trapping experiment, indicating the formation of the characteristic •OH-DMPO adduct (Fig. S2B). These findings, derived from both the IPA-mediated hydroxyl radical scavenging test and EPR analysis, validate the essential involvement of •OH in the

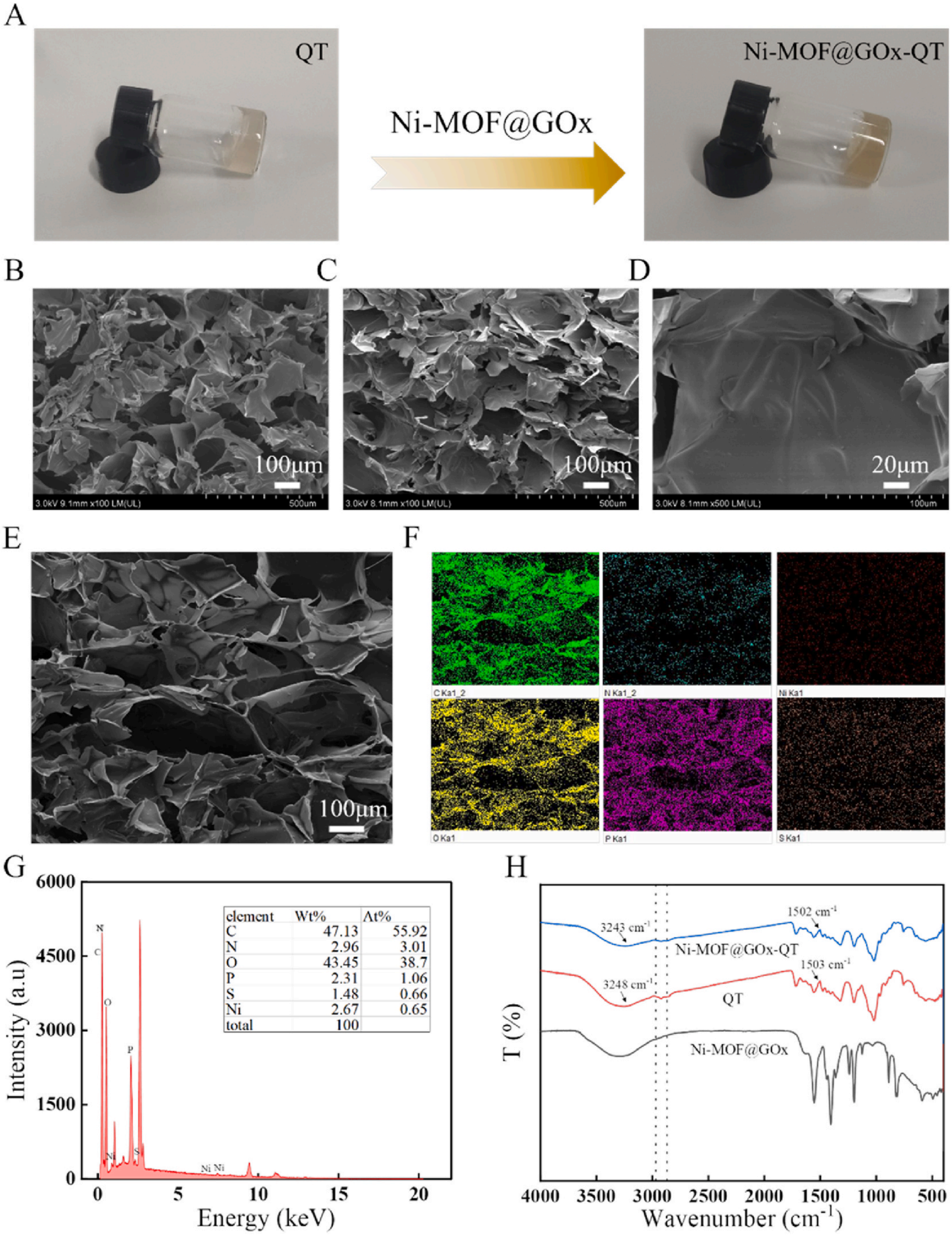

element	Wt%	At%
C	47.13	55.92
N	2.96	3.01
O	43.45	38.7
P	2.31	1.06
S	1.48	0.66
Ni	2.67	0.65
total	100	

Fig. 3. The formation of the Ni-MOF@GOx-QT nanozyme hydrogel by mixing QT hydrogel with Ni-MOF@GOx (A). The SEM images of the QT hydrogel (B) and Ni-MOF@GOx-QT nanozyme hydrogel (C). An enlarged SEM image of the Ni-MOF@GOx-QT nanozyme hydrogel (D). SEM images of Ni-MOF@GOx-QT nanozyme hydrogel, along with corresponding elemental mapping images of C, N, Ni, O, P, and S (E) and (F). The EDS spectrum and elemental composition of the Ni-MOF@GOx-QT nanozyme hydrogel (G). The FT-IR spectra of Ni-MOF@GOx, QT hydrogel, and Ni-MOF@GOx-QT nanozyme hydrogel (H).

catalytic process.

3.4. Synthesis and characterization of hydrogels

The Ni-MOF@GOx-doped QT hydrogel was polymerized through physical crosslinking, resulting in a stable Ni-MOF@GOx-QT nanozyme hydrogel, as illustrated in Fig. 3A. SEM characterization confirmed the hydrogel's three-dimensional network structure, which remained intact despite the incorporation of Ni-MOF@GOx. The SEM images clearly depicted the uniform dispersion of Ni-MOF@GOx within the QT gel

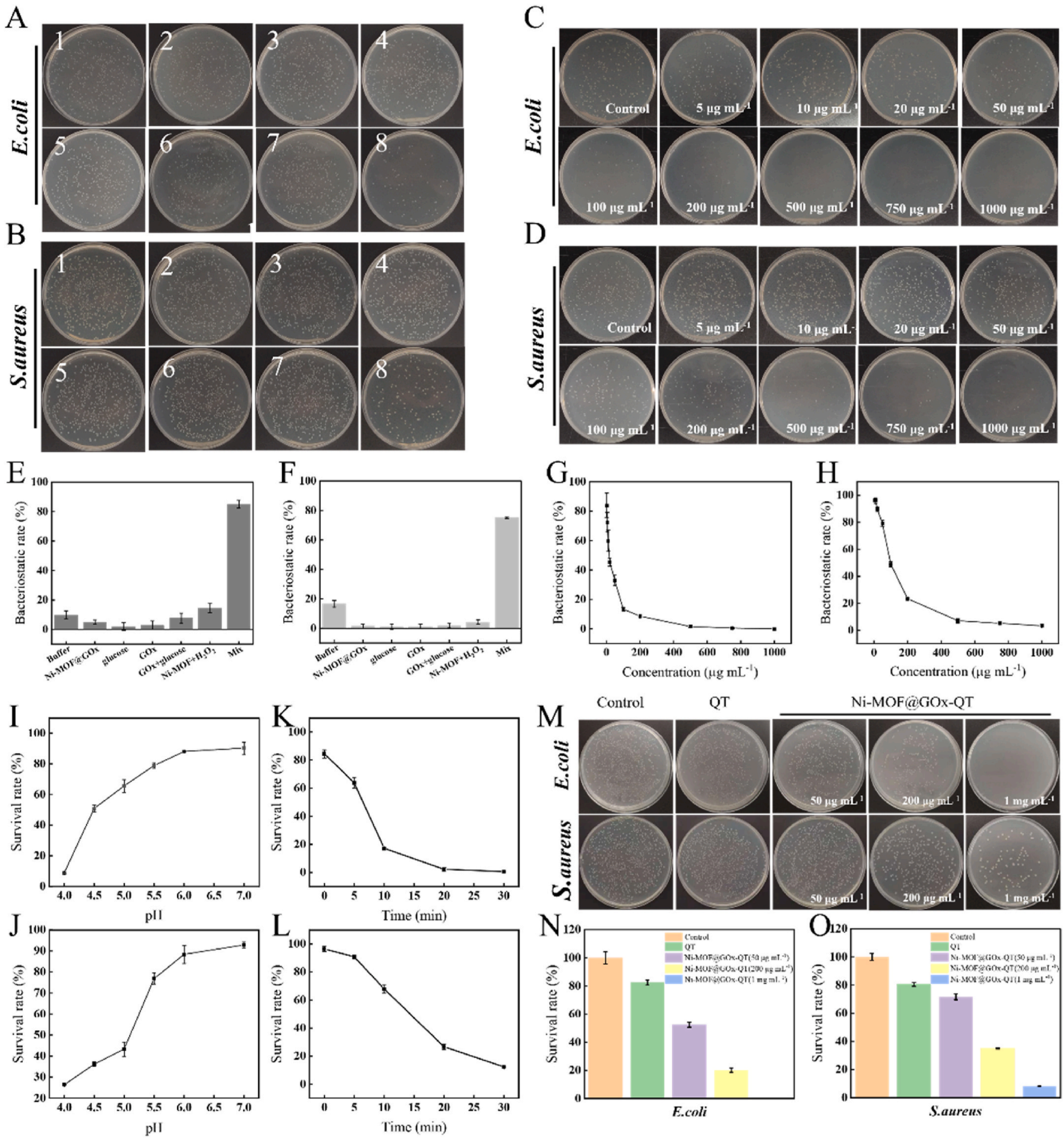

Fig. 4. Bacterial colony images post-treatment for *E. coli* (A) and *S. aureus* (B) across various groups: (1) PBS, (2) Buffer, pH = 4, (3) Ni-MOF@GOx, (4) Glucose, (5) GOx, (6) GOx + glucose, (7) Ni-MOF + H_2O_2, (8) Mix: glucose + Ni-MOF@GOx. *E. coli* and *S. aureus* colony images after treatment with different concentrations of Ni-MOF@GOx (C) and (D). The antibacterial rates for *E. coli* and *S. aureus* across different treatment groups (E) and (F). The antibacterial rates of *E. coli* and *S. aureus* when treated with Ni-MOF@GOx at concentrations ranging from 5 to 1000 μg mL^{-1} (G) and (H). The optimization of Ni-MOF antibacterial activity based on pH and incubation time (I) and (K). The optimization of Ni-MOF@GOx antibacterial activity based on pH and incubation time (J) and (L). Images of bacterial colonies formed after treatment with different experimental groups for *E. coli* and *S. aureus* (M), and the corresponding survival rates for *E. coli* and *S. aureus* (N) and (O).

structure (Fig. 3B–D). Elemental mapping of the Ni-MOF@GOx-QT nanozyme hydrogel (Fig. 3E and F) showed an even distribution of C, N, Ni, O, P, and S throughout the nanomaterial. FT-IR spectra verified the successful doping of Ni-MOF@GOx into the QT hydrogel. In the spectrum of the Ni-MOF@GOx-QT nanozyme hydrogel, the broadening of the O–H peak near 3248 cm^{-1} (Fig. 3H) suggested hydrogen bond formation [30], anchoring Ni-MOF@GOx to the QT hydrogel. Additionally, the broadening of the absorption band at 1502 cm^{-1} upon GOx loading indicated the formation of C=O, further confirming the successful preparation of the hydrogel.

Diabetic wounds, often irregular and associated with deep tissue necrosis, pose challenges in wound management. Studies have demonstrated that injectable hydrogels can effectively fill such irregular wounds, making them a promising option for wound care [31–33]. The practical potential of the Ni-MOF@GOx-QT nanozyme hydrogel was evaluated through adhesion performance testing (Fig. S3A). The results showed excellent tissue adhesion and mechanical adaptability of the hydrogel, allowing it to conform closely to the contours of finger joints and maintain stable attachment during extensive flexion movements without detaching. Further tests confirmed the strong adhesion of the Ni-MOF@GOx-QT hydrogel to various materials, including glass and plastic (Fig. S3B). This exceptional interfacial adhesion can be attributed to the synergistic effects of TA and QC in the hydrogel, whose abundant phenolic hydroxyl and amino groups form non-covalent interactions with different surfaces. These properties suggest significant advantages of the Ni-MOF@GOx-QT nanozyme hydrogel as a wound dressing, eliminating the need for secondary fixation typically required by traditional dressings and reducing mechanical damage to newly formed tissues during dressing changes, thus enhancing patient comfort and treatment efficacy. Additionally, the injectability of the Ni-MOF@GOx-QT nanozyme hydrogel was assessed by loading it into a syringe for extrusion experiments. As depicted in Fig. S3C and Fig. S3D, the hydrogel exhibited good injectability, smoothly extruding through the syringe needle. The successful formation of the letters "WSTK" with the extruded hydrogel confirmed its excellent injectability, indicating potential for in vivo use. In conclusion, the Ni-MOF@GOx-QT nanozyme hydrogel holds promise for application in treating irregular diabetic wounds.

3.5. *Assessment of antimicrobial efficacy in vitro*

The experimental findings previously strongly support the exceptional cascade catalytic performance of Ni-MOF@GOx. This dual-functional mechanism effectively depleted nutrients essential for bacterial growth in wound environments and converted the resulting H_2O_2 into highly oxidative •OH radicals, providing effective antibacterial treatment. The inhibitory effects of Ni-MOF@GOx on *E. coli* and *S.aureus* in the presence of glucose were explored to evaluate its antibacterial properties (Fig. 4A–F). As revealed from the results, 1) the use of either glucose or Ni-MOF@GOx alone did not significantly affect antibacterial activity; 2) the combination of GOx with glucose yielded killing rates of only 7.7 % for *E. coli* and 2.0 % for *S. aureus*; 3) the pairing of Ni-MOF with H_2O_2 exhibited inhibition rates of 14.5 % for *E. coli* and 4.4 % for *S. aureus*; 4) a significant synergistic antibacterial effect appeared when glucose and Ni-MOF@GOx were applied together, with killing rates exceeding 75 % for both *E. coli* and *S. aureus*, suggesting a clear concentration-dependent antibacterial activity of Ni-MOF@GOx (Fig. 4G and H).

The factors influencing the antibacterial activity of both Ni-MOF and Ni-MOF@GOx were optimized. The observed antibacterial trends (Fig. 4I–L) were consistent with the material's POD-like catalytic activity, contributing to the identification of the optimal antibacterial pH (pH 4) and incubation time (20 min). Furthermore, the antibacterial effects of Ni-MOF@GOx-QT nanozyme hydrogels were assessed. Post-treatment experiments with these nanozyme hydrogels demonstrated a significant reduction in bacterial viability for both *E. coli* and *S. aureus*, and inhibition rates exceeded 90 % when treated with 1 mg mL^{-1} Ni-MOF@GOx-QT nanozyme hydrogels (Fig. 4M–O). Thus, they have excellent bactericidal performance.

The biocompatibility of hydrogels is essential for effective wound healing [34,35]. This was evaluated by determining the cytotoxicity of the Ni-MOF@GOx-QT nanozyme hydrogel through the CCK-8 assay with L929 cells as a model. These cells were incubated with hydrogels composed of Ni-MOF@GOx, QT, and the composite Ni-MOF@GOx-QT nanozyme at a concentration of 1 mg mL^{-1} for 24 h. The results suggest that cell viability in all test groups remained above 90 % (Fig. 5A). This finding confirms that the QT hydrogel matrix is non-toxic, Ni-MOF@GOx is biocompatible, and the Ni-MOF@GOx-QT nanozyme hydrogel maintains excellent cellular compatibility, laying a foundation for further in vivo studies.

Further tests involved incubating L929 cells with various concentrations of hydrogels for 24 h, as shown in Fig. 5B. The cell viability in all hydrogel-treated groups exceeded 95 %, similar to the control group. Even at a concentration of 2 mg mL^{-1}, the Ni-MOF@GOx-QT nanozyme hydrogel displayed negligible toxicity to L929 cells. These findings not only reaffirm the hydrogel's biocompatibility but also suggest its potential to enhance cell proliferation. Given the significant roles of fibroblast proliferation and migration in skin wound healing [36–38], additional experiments were conducted to observe the effects of the hydrogels on L929 cell growth. Continuous monitoring over three days revealed that cell proliferation was higher in the QT hydrogel group compared to the control group, likely due to the proliferative properties of TA within the hydrogel. The Ni-MOF@GOx-QT nanozyme hydrogel group showed the most pronounced effect in promoting proliferation, possibly related to the trace metal ions from Ni-MOF@GOx enhancing cell metabolism, as indicated in Fig. 5C. These results suggest that the Ni-MOF@GOx-QT nanozyme hydrogel not only is safe biologically but also facilitates wound healing by stimulating fibroblast proliferation.

Recognizing the critical role of cell migration in wound healing [39–41], the effects of the different materials on cell migration were assessed using the L929 cell scratch assay. The findings, depicted in Fig. 5D and E, indicate that all experimental groups significantly enhanced cell migration compared to the control group. The QT hydrogel group showed moderate migration-promoting effects, achieving approximately 75 % migration efficiency at 48 h. In contrast, the Ni-MOF@GOx-QT nanozyme hydrogel group exhibited the strongest migration-promoting performance, with efficiencies exceeding 90 % at 48 h. This enhanced migration may be attributed to the trace metal ions from Ni-MOF@GOx activating cell migration-related signaling pathways and the antioxidant properties of TA in the hydrogel mitigating the inhibitory effects of oxidative stress on cell migration. These findings suggest that the Ni-MOF@GOx-QT nanozyme hydrogel creates favorable conditions for accelerated wound healing by promoting cell migration.

The *HR* is a crucial metric for assessing the blood compatibility of materials [42,43]. It measures the extent of damage to red blood cell membranes by quantifying the amount of hemoglobin released following interaction with the material. Specifically, when materials cause red blood cells to rupture, hemoglobin is released into the plasma. This release can be quantified by measuring the absorbance of hemoglobin at a wavelength of 540 nm, which is then used to calculate the hemolysis rate.

A higher *HR* indicates more significant damage to the red blood cells caused by the material. Experimental results (Fig. 5F) reveal that the *HR* of the Ni-MOF@GOx-QT nanozyme hydrogel is only 4.12 %, which is below the 5 % safety threshold for biological materials. This suggests a minimal interaction between the hydrogel and red blood cell membranes, indicating that the components of the hydrogel do not cause significant damage to the red blood cells. This compliance with safety standards underscores the hydrogel's suitability for medical use, particularly in wound repair. The favorable blood compatibility of the Ni-MOF@GOx-QT nanozyme hydrogel offers substantial assurance for

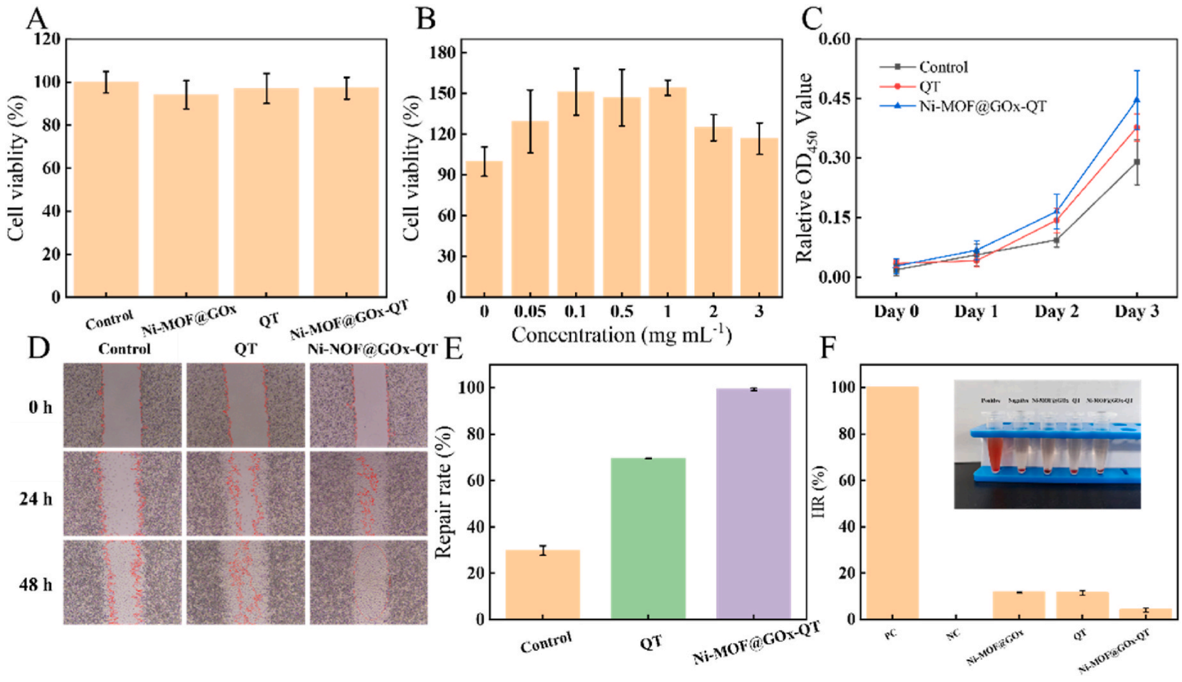

Fig. 5. (A) Cell viability of L929 cells after 24 h of treatment with Ni-MOF@GOx, QT hydrogel, and Ni-MOF@GOx-QT nanozyme hydrogel with the same Ni-MOF@GOx concentration. (B) Cell viability of L929 cells after 24 h of treatment with different concentrations of Ni-MOF@GOx-QT nanozyme hydrogel. (C) OD values of cells in each experimental group over 3 days. (D) Images of scratch assays on L929 cells incubated with different groups for 24 h and 48 h. (E) Corresponding histogram of cell migration rates. (F) Histogram of hemolysis rates of fresh rat red blood cells treated with different experimental groups.

its application in medical treatments.

3.6. Assessment of wound healing

The effectiveness of the Ni-MOF@GOx-QT nanozyme hydrogel in promoting wound healing in diabetic rats was assessed in this study by establishing a 1.5 cm full-thickness skin excision wound model. Observations and measurements were performed on postoperative days 0, 3, 7, 10, and 14 to determine the *WHR*. Fig. 6A reveals that on day 3 post-injury, the wounds in the control group appeared dry, whereas those treated with the nanozyme hydrogel remained moderately moist. Between days 3 and 7, the control group's wounds developed thick, dry scabs; the scabs in the Ni-MOF@GOx-QT nanozyme hydrogel-treated group were softer. On days 7–10, the control group's scabs were rough and hard, indicating edge detachment. In contrast, the scabs in the hydrogel-treated group had completely detached by this time, revealing pink, moist granulation tissue. By day 14, there was a noticeable reduction in wound size across all groups, and the control group exhibited a significantly larger unhealed area compared to the nearly fully healed wounds in the hydrogel group. Thus, the Ni-MOF@GOx-QT nanozyme hydrogel significantly can enhance wound healing in diabetic rats, improve the wound microenvironment, and accelerate tissue regeneration.

Further analysis based on the measurements of wound area (Fig. 6B) and *WHR* (Fig. 6C) presents a gradual decrease in wound size and a continuous increase in WHR across all groups. By day 7 post-injury, a significant difference in the healing rates appeared. Between days 7 and 10, the hydrogel group exhibited a WHR of 92.63 %, which was significantly higher than that of the control group. By day 14, the WHR reached 98.88 % in the hydrogel group and only 78.99 % in the control group. According to clinical standards, a WHR above 95 % is considered indicative of complete healing. Thus, by day 14, the wounds in the hydrogel group had effectively healed, whereas the wounds in the control group had not met these healing criteria. These findings underscore that the Ni-MOF@GOx-QT nanozyme hydrogel dressing notably accelerated wound healing, facilitating the wound repair process and providing vital experimental evidence for the treatment of diabetes-related wounds. Moreover, this hydrogel dressing maintains an optimal moist environment conducive to wound healing and demonstrates efficient absorption of tissue exudate [44–46], further promoting the healing process.

The rats' body weight during the experimental period was monitored (Fig. 6D), suggesting a slow and steady growth trend across all three groups, with no significant differences observed. In other words, the Ni-MOF@GOx-QT nanozyme hydrogel did not negatively impact the normal growth and development of the rats, further confirming its biocompatibility and safety.

The analysis of the wound healing process based on HE staining of post-injury tissue samples (Fig. 6E) unveiled distinct differences between the groups. By the third day post-injury, all groups exhibited loosely arranged and disordered collagen fibers in the dermis, along with significant inflammatory cell infiltration. Nonetheless, the group treated with Ni-MOF@GOx-QT nanozyme hydrogel demonstrated new blood vessel formation, and the control group presented a disorganized arrangement of epidermal spinous layer cells, increased bleeding points, and a thickened epidermis. By day 7 post-injury, the abnormal skin tissue structure persisted in the control group, marked by disorganized arrangements and ongoing inflammation. In contrast, the nanozyme hydrogel group displayed trends towards a normal skin structure, with abundant new blood vessels and hair follicles, regardless of the loosely arranged collagen fibers. By day 10, the control group still had disarray in collagen fibers and continued inflammatory cell presence, whereas the Ni-MOF@GOx-QT nanozyme hydrogel group possessed more orderly arranged collagen fibers and evidence of neovascularization. By day 14, limited inflammatory cell infiltration continued in the control group, and the nanozyme hydrogel group exhibited a thickened epidermis, follicle generation, and tightly organized collagen fibers, as well as a skin tissue structure resembling that of normal skin. These results imply that the Ni-MOF@GOx-QT nanozyme hydrogel can effectively promote wound tissue repair, improve collagen arrangement, and facilitate the normalization of skin structure.

A systematic analysis of tissue repair at various time points following

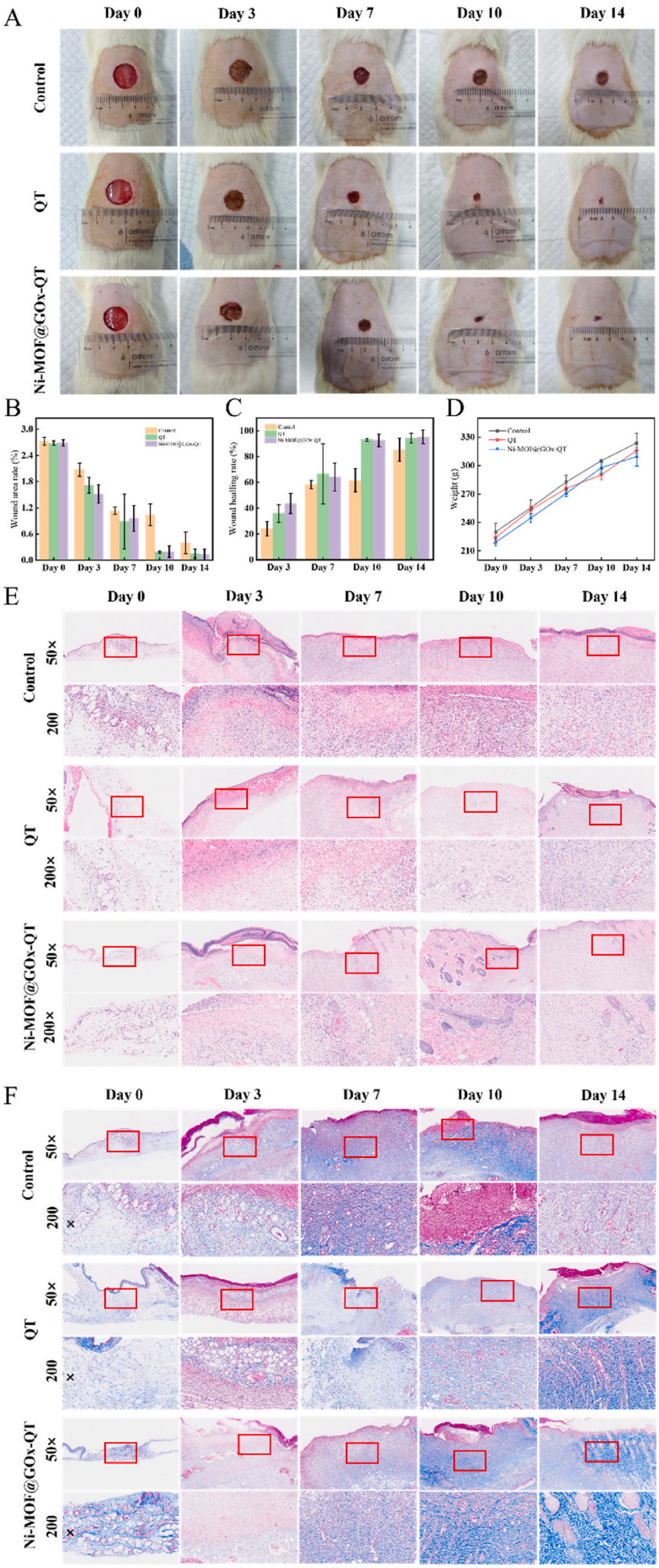

Fig. 6. The morphological changes in wounds of SD rats at various time intervals (A), the progression of wound areas from day 0 to day 14 (B), the healing rates over 14 days (C), changes in rats' body weight during the treatment period (D), and histological images of wound tissues stained with HE and Masson's trichrome at different time points (0–14 days) for each group (E and F).

injury was conducted based on the results of Masson staining (Fig. 6F). On day 0, all groups presented full-thickness skin defects and mild inflammatory responses. By day 3, extensive collagen degeneration and necrosis were observed in both the control group and the QT hydrogel group, and the Ni-MOF@GOx-QT nanozyme hydrogel group exhibited only localized collagen degradation and moderate swelling. By day 7, the control group manifested some reduction in collagen degeneration, and the Ni-MOF@GOx-QT group displayed signs of neovascularization with distinct dermal boundaries, even though the collagen fibers remained disorganized. On day 10, the control group had significantly less new collagen compared to the Ni-MOF@GOx-QT group, reflecting a trend toward organized collagen fiber alignment. By day 14, the control group revealed limited new collagen formation with some degree of organization; the QT hydrogel group had a notably higher collagen content compared to the control group; the Ni-MOF@GOx-QT group presented the most optimal tissue repair outcome, with the highest collagen content and an intact dermal structure featuring orderly aligned collagen fibers, similar to normal skin tissue. Hence, the Ni-MOF@GOx-QT nanozyme hydrogel has the potential to enhance wound healing.

4. Conclusions

In this study, Ni-MOF@GOx nanomaterials with cascade enzyme catalytic activity were successfully synthesized. These materials efficiently converted H_2O_2 into •OH under acidic conditions, demonstrating significant bactericidal effects against *E. coli* and *S. aureus*. Additionally, the use of QT hydrogel as a carrier for Ni-MOF@GOx improved biocompatibility. Ni-MOF@GOx effectively disinfected wounds while providing a protective barrier against bacterial invasion in combination with QT hydrogel. Moreover, the injectability of the hydrogel was verified as particularly advantageous for treating irregularly shaped wounds. Ni-MOF@GOx-QT nanozyme hydrogels promoted cell migration and proliferation, accelerating wound healing. Furthermore, in vivo experiments further confirmed the role of Ni-MOF@GOx-QT nanozyme hydrogels in the healing of diabetic and bacterially infected wounds, highlighting their potential for rapid wound disinfection, effective sterilization, accelerated healing, and skin repair.

CRediT authorship contribution statement

Wenbin Zhong: Writing – original draft, Methodology, Investigation, Data curation. **Dongying An:** Writing – original draft, Methodology, Investigation, Data curation. **Zhiyu Ma:** Supervision, Funding acquisition. **Jin Li:** Funding acquisition. **Nishan Jin:** Investigation. **Yutian Zhou:** Investigation. **Murui Ying:** Investigation. **Xin Li:** Funding acquisition. **Song Gao:** Supervision, Conceptualization. **Bo Hu:** Writing – review & editing, Supervision, Funding acquisition, Conceptualization. **Yang Zhang:** Writing – review & editing, Supervision, Funding acquisition, Conceptualization.

Ethical statement

All animal experiments were approved by the Animal Ethics Committee of The Affiliated Hospital of Shenyang Medical College.

Declaration of competing interest

The authors declare that they have no known competing financial interests or personal relationships that could have appeared to influence the work reported in this paper.

Acknowledgements

The authors appreciate financial supports from the Shenyang Science and Technology Talent Special Project (RC230022), Liaoning Provincial Department of Education (LJ222100164024), Natural Science Foundation Joint Fund of Liaoning Province (2023-MSLH-288, 2023-BSBA-299), Liaoning Province Science and Technology Plan Project (2023JH2/20200088), Shenyang Medical College Project (SYKT2025002, SYKT2025004 and SYKT2025005).

Appendix A. Supplementary data

Supplementary data to this article can be found online at https://doi.org/10.1016/j.talanta.2025.128690.

Data availability

Data will be made available on request.

References

[1] F. Mariani, M. Serafini, I. Gualandi, D. Arcangeli, F. Decataldo, L. Possanzini, et al., Advanced wound dressing for real-time pH monitoring, ACS Sens. 6 (2021) 2366–2377.

[2] S. Shi, X. Ou, J. Long, X. Lu, S. Xu, L. Zhang, Nanoparticle-based therapeutics for enhanced burn wound healing: a comprehensive review, Int. J. Nanomed. 19 (2024) 11213–11233.

[3] O.O. Olutoye, E. Eriksson, A.D. Menchaca, R.S. Kirsner, R. Tanaka, G. Schultz, et al., Management of acute wounds-expert panel consensus statement, Adv. Wound Care 13 (2024) 553–583.

[4] Y. Huang, J. Ren, X. Qu, Nanozymes: classification, catalytic mechanisms, activity regulation, and applications, Chem. Rev. 119 (2019) 4357–4412.

[5] Y. Zhang, D. Li, J. Tan, Z. Chang, X. Liu, W. Ma, et al., Near-infrared regulated nanozymatic/photothermal/photodynamic triple-therapy for combating multidrug-resistant bacterial infections via oxygen-vacancy molybdenum trioxide nanodots, Small 17 (2021) e2005739.

[6] M. Velumani, G. Thiruppathi, A. Mohankumar, D. Kalaiselvi, P. Sundararaj, P. Premasudha, Green synthesis of zinc oxide nanoparticles using Cananga odorata essential oil and its antibacterial efficacy in vitro and in vivo, Comp. Biochem. Physiol. C Toxicol. Pharmacol. 262 (2022) 109448.

[7] H. Yang, N. Chen, Z. Wang, J. Liu, J. Qin, K. Zhu, et al., Biochar-associated free radicals reduce soil bacterial diversity: new insight into ecoenzymatic stoichiometry, Environ. Sci. Technol. 57 (2023) 20238–20248.

[8] M. Zhai, P. Gong, H. Li, J. Peng, W. Xu, S. Song, et al., Metastable interface biomimetic synthesis of a smart nanosystem for enhanced starvation/gas therapy, J. Colloid Interface Sci. 599 (2021) 149–157.

[9] Y. Chen, H. Cao, C. Jiang, Y. Li, Tumor-microenvironment-mediated second near-infrared light activation multifunctional Cascade nanoenzyme for self-replenishing O(2)/H(2)O(2) multimodal tumor therapy, J. Colloid Interface Sci. 683 (2024) 930–943.

[10] L. Chen, S. Xing, Y. Lei, Q. Chen, Z. Zou, K. Quan, et al., A glucose-powered activatable nanozyme breaking pH and H(2) O(2) limitations for treating diabetic infections, Angew Chem. Int. Ed. Engl. 60 (2021) 23534–23539.

[11] S. Li, S. Dong, W. Xu, S. Tu, L. Yan, C. Zhao, et al., Antibacterial hydrogels, Adv. Sci. (Weinh.) 5 (2018) 1700527.

[12] Y. Xiao, Y. Gu, L. Qin, L. Chen, X. Chen, W. Cui, et al., Injectable thermosensitive hydrogel-based drug delivery system for local cancer therapy, Colloids Surf. B Biointerfaces 200 (2021) 111581.

[13] H. Zhao, M. Liu, Y. Zhang, J. Yin, R. Pei, Nanocomposite hydrogels for tissue engineering applications, Nanoscale 12 (2020) 14976–14995.

[14] W. Chen, Y. Ming, M. Wang, M. Huang, H. Liu, Y. Huang, et al., Nanocomposite hydrogels in regenerative medicine: applications and challenges, Macromol. Rapid Commun. 44 (2023) e2300128.

[15] H. Luo, X.Q. Yin, P.F. Tan, Z.P. Gu, Z.M. Liu, L. Tan, Polymeric antibacterial materials: design, platforms and applications, J. Mater. Chem. B 9 (2021) 2802–2815.

[16] P. Deng, F. Chen, H. Zhang, Y. Chen, J. Zhou, Conductive, self-healing, adhesive, and antibacterial hydrogels based on Lignin/Cellulose for rapid MRSA-Infected wound repairing, ACS Appl. Mater. Interfaces 13 (2021) 52333–52345.

[17] T. Distler, A.R. Boccaccini, 3D printing of electrically conductive hydrogels for tissue engineering and biosensors - a review, Acta Biomater. 101 (2020) 1–13.

[18] H. Wang, X. Wang, K. Lai, J. Yan, Stimulus-responsive DNA hydrogel biosensors for food safety detection, Biosensors (Basel) 13 (2023).

[19] A. Hassen, E.A. Moawed, R. Bahy, A.B. El Basaty, S. El-Sayed, A.I. Ali, et al., Synergistic effects of thermally reduced graphene oxide/zinc oxide composite material on microbial infection for wound healing applications, Sci. Rep. 14 (2024) 22942.

[20] H. Zhang, Y. Zhang, Y. Zhang, H. Li, M. Ou, Y. Yu, et al., Catalytic activity of violet phosphorus-based nanosystems and the role of metabolites in tumor therapy, Nat. Commun. 15 (2024) 6783.

[21] Y. Chen, Y. Chen, Z. Wang, L. Yang, Y. Zhang, Z. Zhang, et al., Iron-based MOF with catalase-like activity improves the synergistic therapeutic effect of PDT/ferroptosis/starvation therapy by reversing the tumor hypoxic microenvironment, J. Nanobiotechnol. 22 (2024) 705.

[22] P. Le Thi, D.L. Tran, Thi TT. Hoang, Y. Lee, K.D. Park, Injectable reactive oxygen and nitrogen species-controlling hydrogels for tissue regeneration: current status and future perspectives, Regen. Biomater. 9 (2022) rbac069.

[23] M. Zhang, X. Yao, J. Xu, J. Song, S. Mai, W. Zhu, et al., Biodegradable zwitterionic polymer-cloaked defective metal-organic frameworks for ferroptosis-inducing cancer therapy, Int. J. Pharm. 655 (2024) 124032.

[24] T.H.Y. Beglau, L. Rademacher, R. Oestreich, C. Janiak, Synthesis of ketjenblack decorated pillared Ni(Fe) metal-organic frameworks as precursor electrocatalysts for enhancing the oxygen evolution reaction, Molecules 28 (2023).

[25] P.S. Bagus, C.J. Nelin, S.T. Mergelsberg, N. Lahiri, E.S. Ilton, Chemical information from XPS: theory and experiment for Ni(OH)2, J. Chem. Phys. 161 (2024).

[26] W. Tan, T. Wei, J. Huo, M. Loubidi, T. Liu, Y. Liang, et al., Electrostatic interaction-induced formation of Enzyme-on-MOF as chemo-biocatalyst for Cascade reaction with unexpectedly acid-stable catalytic performance, ACS Appl. Mater. Interfaces 11 (2019) 36782–36788.

[27] C. Yang, W. Liu, S. Chen, X. Zong, P. Yuan, X. Chen, et al., MOF-immobilized two-in-one engineered enzymes enhancing activity of biocatalytic Cascade for tumor therapy, Adv. Healthcare Mater. 12 (2023) e2203035.

[28] X. Lian, Y. Fang, E. Joseph, Q. Wang, J. Li, S. Banerjee, et al., Enzyme-MOF (metal-organic framework) composites, Chem. Soc. Rev. 46 (2017) 3386–3401.

[29] J. Yang, Y.W. Yang, Metal-organic frameworks for biomedical applications, Small 16 (2020) e1906846.

[30] H. Hamedi, S. Moradi, S.M. Hudson, A.E. Tonelli, Chitosan based hydrogels and their applications for drug delivery in wound dressings: a review, Carbohydr. Polym. 199 (2018) 445–460.

[31] X. Zhao, H. Wu, B. Guo, R. Dong, Y. Qiu, P.X. Ma, Antibacterial anti-oxidant electroactive injectable hydrogel as self-healing wound dressing with hemostasis and adhesiveness for cutaneous wound healing, Biomaterials 122 (2017) 34–47.

[32] X. Lan, T. Du, J. Zhuo, T. Wang, R. Shu, Y. Li, et al., Advances of biomacromolecule-based antibacterial hydrogels and their performance evaluation for wound healing: a review, Int. J. Biol. Macromol. 279 (2024) 135577.

[33] P. Wang, Q. Zhang, S. Wang, D. Wang, R.C.S. Yip, W. Xie, et al., Injectable salecan/Hyaluronic acid-based hydrogels with antibacterial, rapid self-healing, pH-responsive and controllable drug release capability for infected wound repair, Carbohydr. Polym. 347 (2025) 122750.

[34] J. Ma, T. Li, M. Luo, B. Lei, Single-component self-healing antibacterial anti-inflammatory intracellular-antioxidative poly(itaconic acid-pluronic) hydrogel for rapid repair of MRSA-impaired wound, ACS Appl. Mater. Interfaces 15 (2023) 33413–33424.

[35] M. Wang, T. Li, J. Tian, L. Zhang, Y. Wang, S. Li, et al., Engineering single-component antibacterial anti-inflammatory Polyitaconate-Based hydrogel for promoting methicillin-resistant staphylococcus aureus-infected wound healing and skin regeneration, ACS Nano 18 (2024) 395–409.

[36] M.A. Koo, Hong S. Hee, M. Hee Lee, B.J. Kwon, Seon G. Mi, Kim M. Sung, et al., Effective stacking and transplantation of stem cell sheets using exogenous ROS-Producing film for accelerated wound healing, Acta Biomater. 95 (2019) 418–426.

[37] L. Maeso, P.E. Antezana, A.G. Hvozda Arana, P.A. Evelson, G. Orive, M. F. Desimone, Progress in the use of hydrogels for antioxidant delivery in skin wounds, Pharmaceutics 16 (2024).

[38] G. Olteanu, S.M. Neacşu, F.A. Joiţa, A.M. Musuc, E.C. Lupu, C.B. Ioniţă-Mîndrican, et al., Advancements in regenerative hydrogels in skin wound treatment: a comprehensive review, Int. J. Mol. Sci. 25 (2024).

[39] F. Mascarenhas-Melo, D. Peixoto, C. Aleixo, S.G. Mb, F. Raza, K.D. Pawar, et al., Nanoclays for wound management applications, Drug Deliv Transl Res 13 (2023) 924–945.

[40] W. Dou, X. Zeng, S. Zhu, Y. Zhu, H. Liu, S. Li, Mussel-Inspired injectable adhesive hydrogels for biomedical applications, Int. J. Mol. Sci. 25 (2024).

[41] Y. Gu, Y. You, Y. Yang, X. Liu, L. Yang, Y. Li, et al., Multifunctional EGCG@ZIF-8 nanoplatform with photodynamic Therapy/Chemodynamic therapy antibacterial properties promotes infected wound healing, ACS Appl. Mater. Interfaces 16 (2024) 50238–50250.

[42] X. Zhang, Y. Mu, L. Zhao, Y. Hong, L. Shen, Self-healing, antioxidant, and antibacterial Bletilla striata polysaccharide-tannic acid dual dynamic crosslinked hydrogels for tissue adhesion and rapid hemostasis, Int. J. Biol. Macromol. 270 (2024) 132182.

[43] B.D. Ratner, The catastrophe revisited: blood compatibility in the 21st Century, Biomaterials 28 (2007) 5144–5147.

[44] Y. Fan, M. Zhan, J. Liang, X. Yang, B. Zhang, X. Shi, et al., Programming injectable DNA hydrogels yields tumor microenvironment-activatable and immune-instructive depots for augmented chemo-immunotherapy, Adv. Sci. (Weinh.) 10 (2023) e2302119.

[45] L. Sun, F. Shen, L. Tian, H. Tao, Z. Xiong, J. Xu, et al., ATP-Responsive smart hydrogel releasing immune adjuvant synchronized with repeated chemotherapy or radiotherapy to boost antitumor immunity, Adv. Mater. 33 (2021) e2007910.

[46] H. Zhou, Y. Zhu, B. Yang, Y. Huo, Y. Yin, X. Jiang, et al., Stimuli-responsive peptide hydrogels for biomedical applications, J. Mater. Chem. B 12 (2024) 1748–1774.